Atmospheric
Chemistry
and Physics

Supplement of

Volatile oxidation products and secondary organosiloxane aerosol from $D_5 + OH$ at varying OH exposures

Hyun Gu Kang et al.

Correspondence to: Thomas Berkemeier (t.berkemeier@mpic.de) and Hwajin Kim (khj0116@snu.ac.kr)

S1 Experiment and Set Up Details

S1.1 PAM-OFR

Fig. S1 shows the experiment set up. During these experiments, the laboratory room temperatures and pressures were 17 – 21 °C and ~1020 hPa (1 atm) respectively. In this manuscript, we used 1 atm for unit conversions and in KinSim. We passed different flow ratios of dry and humid zero air through the passivated 15 mL glass bulb to get the desired experiment humidity conditions. Mass flow controllers (MFC, MC and MCS series, Alicat Scientific, Tucson, AZ, USA) controlled the input air flow rates. Air coming out of the PAM-OFR and instrument outlets went to the exhaust or through scrubbers to minimize O_3 and aerosol exposure in the room. Ultra-high purity N_2 from a gas cylinder (Sinyang Oxygen Company, Seoul, South Korea) regulated to 30 psig purged the UV lamps.

The PAM-OFR was connected to an O_3 monitor (Model UV-100, 2B Technologies, Boulder, CO, USA) via the outlet side port. For the 120 s τ_{res} experiment, a pump was attached to the outlet side port for additional flow. The PTR-MS inlet and the aerosol sampling line was connected at the OFR outlet center port (Fig. S1). We used perfluoroalkoxy alkane (PFA) tubing (6.35 mm (1/4") OD, 4.35 mm ID, Sungjin Rubber Industrial, Seoul, South Korea) for the connections to the OFR inlet. The OFR was equipped with conductive Teflon flow rings at both the inlet and the outlet side ports, and the D_5 and humid air were injected through the inlet side port.

We used D_5 (97 %, CAS#541-02-6, Sigma-Aldrich, Saint Louis, MO, USA) as the VOC precursor and stored the D_5 in a refrigerator (~1 °C) when not in use. A syringe pump (Fusion 4000, Chemyx, Stafford, TX, USA) equipped with a 10 uL gas-tight microliter syringe (Model 1801, Hamilton, Reno, NV, USA) continuously injected D_5 into the PAM-OFR. The syringe fed into the passivated glass bulb through a polytetrafluoroethylene-faced (PTFE) septa (13 mm, Scilab, Seoul, South Korea) at room temperature. At the injection speeds and air flow rates used, we did not visually observe any D_5 build-up in the bulb.

For cleaning, making atomizer solutions, and generating humid air for the PAM-OFR, we used Type 1 deionized water (DI water, >18.2 MΩ cm resistivity at 25 °C) from a purification system (Milli-Q Direct 16, Merck, Darmstadt, Germany). We rinsed the microliter syringe between experiments with acetone and DI water and dried them at room temperature in the fume hood. The passivated glass bulb was also rinsed with acetone and DI water and heated in a drying oven before the experiments.

Zero air came from a generator (Model 8301P, Acoem Ecotech, Victoria, Australia) coupled with a catalytic converter set to 520 °C (Model HTO-1000HC, Acoem Ecotech, Victoria, Australia). The zero air also passed through scrubbers filled with

activated molecular sieves (4 Å 4 – 8 mesh, Sigma-Aldrich, Saint Louis, MO, USA), $NaMnO_4$ oxidizing media (Purafil SP, Purafil, Doraville, GA, USA), and activated carbon (Purakol, Purafil, Doraville, GA, USA). Lastly, the zero air went through a filtered air supply (Model 3074B, TSI, Shoreview, MN, USA) prior to injection to the PAM-OFR and the Nafion humidifier (FC-100-80-6MKK, Perma Pure, Lakewood, NJ, USA).

To assess the OH_{exp} range, we conducted an offline calibration on the PAM-OFR with calibration CO gas (UnionGas, Gyeonggi-do, South Korea) with a Serinus 30i CO analyzer (Acoem Ecotech, Victoria, Australia). We used humidity conditions close to that of the experiments (Fig. S2). We used the D_5 siloxane trace as a direct measure of OH_{exp} during the experiments themselves and found the OH_{exp} assessed with D_5 to be consistent with the offline calibration with CO. We did not operate the CO analyzer during the experiments to avoid the risk of siloxanes fouling its catalytic converter (Dewil et al., 2006).

S1.2 Aerosol Sampling Line

The aerosol sampling line was connected at the PAM-OFR center outlet port and lead to the SMPS. The sampling line consisted of a O_3 denuder and a Nafion dryer (PD-200T-12MSS, Perma Pure, Lakewood, NJ, USA) with conductive connections and fittings in between. We installed the O_3 denuder in the sampling line to prevent O_3 damage to the SMPS, and it was a diffusion denuder filled with hopcalite pellets (3 mm, Purelyst MD-101, Pure Sphere, Chungcheongnam-do, South Korea). The custom-made diffusion denuder was cylindrical in shape at 52 cm long and 6.5 cm in diameter, and the wet particles would pass through a 12.7 mm (1/2") ID center line made of stainless mesh. Prior to experiments, we passed filtered compressed air through the O_3 denuder at 10 L min^{-1} for ~30 min to remove any loose particles.

We assessed the O_3 removal by comparing the concentrations entering and exiting the O_3 denuder filled with fresh hopcalite pellets. The flow rate through the O_3 denuder matched that of experiments (3.0 L min^{-1}), and we used the same O_3 monitor used on the PAM-OFR. To generate O_3, humid air was fed into the OFR with 185 nm lights on without siloxanes or seed, and the OFR outputted 2.1 ppm of O_3. We found that the denuder would remove ~90 % of the O_3 by concentration at these test conditions.

We used the particle loss calculator (von der Weiden et al., 2009) with the dimensions of the aerosol sampling line to calculate the size dependent losses in the line (Fig. S3). Given that we did not know at what point when the SOSiA was formed in the PAM-OFR, we only applied the particle loss in the aerosol sampling line to correct the Y_{SOSiA}. The particle loss corrections to the Y_{SOSiA} were done by applying the particle loss at the experiment SOSiA volume mode with that from the calculator.

To prevent siloxane contamination from conductive silicone tubing (Timko et al., 2009; Yu et al., 2009; Asbach et al., 2016), we used conductive PFA tubing (6.35 mm (1/4") OD, 4.76 mm (3/16") ID, Fluorotherm Polymers, Parsippany, NJ, USA) and stainless-steel compression fittings for the connections in the aerosol sampling line. In this experiment set up, we only used conductive silicone tubing (12 cm, 9.53 mm (0.375") OD, 4.8 mm (0.19") ID, TSI, Shoreview, MN, USA) at the inlet of the SMPS and for connections between the SMPS components.

S1.3 Condensational Sink and Condensation Lifetimes

We follow the instructions in Section 3.3 of Palm et al. (2016) to calculate the condensational sink (CS, s^{-1}) and low-volatile organic compound (LVOC) condensation lifetimes (τ_{CS}, s), where we use the particle number size distribution from the SMPS. In Eq. (S1), r is the wet particle radius (m), N is the particle number size distribution (m^{-3} at each particle diameter), and β is the dimensionless Fuchs-Sutugin correction factor (Seinfeld and Pandis, 2006). We also use the same gas diffusion coefficient (D_g) used by Palm et al. (2016) of 7×10^{-6} m^2 s^{-1}, which represents LVOC. In Eq. (S3), α is the dimensionless accommodation coefficient that is assumed to be 1 (Liu et al., 2019).

$$CS = 4\pi D_g \int_0^\infty r\beta(r)N(r)dr = 4\pi D_g \sum_0^\infty r\beta(r)N(r) \tag{S1}$$

$$\tau_{CS} = \frac{1}{CS} \tag{S2}$$

$$\beta(r) = \frac{Kn+1}{0.377Kn+1+\frac{4}{3}\alpha^{-1}Kn^2+\frac{4}{3}\alpha^{-1}Kn} \tag{S3}$$

To obtain β, we calculate the dimensionless Knudsen number (Kn), the mean free path (λ_g, m), and the mean thermal velocity (ω_{avg}, m s^{-1}) for LVOC at each r. In Eq. (S6), T refers to the temperature (K) in the PAM-OFR and R is the gas constant (R = 8.3145 kg m^2 s^{-2} K^{-1} mol^{-1}). Since particles were dried before being detected by the SMPS, we obtain r in Eq. (S1) and (S4) by multiplying the dry particle radius with the growth factor (GF), which is the ratio of the wet particle diameter versus when the particle is dry (Fig. S5).

$$Kn = \frac{\lambda_g}{r} \tag{S4}$$

$$\lambda_g = \frac{3D_g}{v_{avg}} \tag{S5}$$

$$\omega_{avg} = \sqrt{\frac{8RT}{\pi M}} \tag{S6}$$

We find GF with Eq. (S7), where κ is the dimensionless hygroscopicity parameter and α_w is the dimensionless water activity approximated via $\alpha_w = \text{RH \%}/100$. For κ, Palm et al. (2016) used a value representing that of SOA ($\kappa = 0.13$), but Janechek et al. (2019) found SOSiA to be non-hygroscopic ($\kappa = 0.01$). Consequently, we calculate the CS for both the LVOC and SOSiA cases, with molecular weights (M) of LVOC, 0.200 kg mol^{-1}, and of D$_5$, 0.370 kg mol^{-1}. The calculated GF for both cases are shown in Fig. S5 and Table S3.

$$\kappa = (GF^3 - 1)(1 - \alpha_w)\alpha_w^{-1} \tag{S7}$$

The PAM-OFR has an estimated LVOC eddy diffusion wall loss lifetime (τ_{wall}) of 400 s (Palm et al., 2016), while the calculated τ_{CS} ranged up to ~136 s when using the particle size distribution measured during experiments (Table S3). Palm et al. (2016) recommended using the average of the particle size distributions entering and exiting the OFR, which would double the aforementioned τ_{CS} since we did not use seed aerosol. Either case, we expect the loss of LVOC to the walls to have been small since $\tau_{CS} < \tau_{wall}$.

S1.4 PTR-MS Inlet and Settings

The PTR-MS inlet was made of SilcoNert 2000-coated (SilcoTek, Bellefonte, PA, USA) stainless steel inlet tubing (1.59 mm (1/16") OD, 1.0 mm (0.040") ID) at 1.2 m in length. The PTR-MS was connected immediately at the center outlet of the OFR with SilcoNert 2000-coated fittings (Swagelok, Solon, OH, USA) and conductive PFA tubing (Fluorotherm Polymers, Parsippany, NJ, USA). We set the flow rate into the PTR-MS inlet to 0.43 L min^{-1} using its built-in inlet flow controller and inlet pressure controller. The PTR-MS inlet was equipped with a heating hose set to 60 °C and a dust filter to prevent clogging, especially at the high SOSiA masses. The single stage filter holder was made of PFA (Savillex, Eden Prairie, MN, USA) and held a 25 mm PTFE filter (5 µm pore, Synspec, Groningen, Netherlands) that was replaced daily.

The mass spectrometer extraction time and maximum flight times were 2.0 and 20.0 µs respectively, with the maximum mass at m/z 632.0. The mass spectra were integrated and recorded every 1000 ms. For the PTR-MS mass scale calibration, we used (H$_2^{18}$O)H$^+$ (m/z 21.0221), (H$_2$O)$_2$H$^+$ (m/z 37.0284), (C$_6$H$_4$I)H$^+$ (m/z 203.9431), and (C$_6$H$_4$I$_2$)H$^+$ (m/z 330.8475) during the data analysis. We used ioniTOF 4.0 to control the instrument and PTR-MS Viewer 3.4.4 (Ionicon Analytik, Innsbruck, Austria) to process the PTR-MS mass spectra.

S1.5 PTR-MS Mass Spectra Interpretation

D$_5$ has isotopologues (Fig. 1) whose ion masses overlap with those of VOP. Additionally, large alcohols fragment during the PTR (Brown et al., 2010), and the reported siloxanol (D$_4$T(OH)) or siloxanediol (D$_3$T$_2$(OH)$_2$) may have fragmented if they

behave like saturated organic alcohols. Since we did not have siloxanol calibration standards, we opt to use the -H_2O fragmentation behavior of organic alcohols to assess the qualitative trends of the proposed VOP.

We use the -H_2O fragment of $[D_4T(OH)]H^+$ at m/z 355, the -H_2O fragment of $D_3T_2(OH)_2$ at m/z 357, and the -H_2O fragment of $[D_3T_2(OH)(OCHO)]H^+$ at m/z 385 to assess the relative trends of these VOP (Table S4). However, the signal at m/z 355 overlaps with the -CH_4 fragment of protonated D_5 $[C_9H_{27}O_5Si_5]^+$, as noted by Coggon et al. (2018). As for m/z 357, this signal overlaps with an isotopologue of the -CH_4 fragment of $[D_5]H^+$ and the -H_2O fragment of $[D_4T(OH)]H^+$. To retrieve the signal of $D_4T(OH)$ and $D_3T_2(OH)_2$, we subtract the fragment and/or isotopologue signals from the total signal at the designated ion masses. For m/z 355, we subtract the -CH_4 fragment of $[D_5]H^+$ using the signal ratios of D_5 at m/z 355 and m/z 371 found prior to each experiment. For m/z 357, we subtract the $[C_9H_{27}O_5Si_5]^+$ isotopologue signal fraction.

For the quantification of D_5, we opt to use the main D_5 ion ($[C_{10}H_{30}Si_5]H^+$) at m/z 371, as opposed to the -CH_4 fragment ion at m/z 355. Coggon et al. (2018) used the fragment ion for their ambient air measurements due to higher ion counts there. $[C_9H_{27}O_5Si_5]^+$ had a higher ion count than $[C_{10}H_{30}Si_5]H^+$ during our calibrations and experiments as well, but the D_5 concentrations in these experiments are sufficiently high for quantification at m/z 371. Additionally, Since the -H_2O fragment ion of $[D_4T(OH)]H^+$ has the same elemental composition of the -CH_4 fragment of $[D_5]H^+$, we choose the m/z 371 ion to avoid potential overlaps in the D_5 quantification.

The PTR-MS is limited in the species it can detect and resolve. The PTR-MS configuration restricts the volatility range of identifiable species, where species are not fragmented during the PTR or lost on the surfaces of the instrument and inlet. Moreover, the PTR is known to fragment peroxides (Li et al., 2022), which limits their detection. Saturated alcohols larger than ethanol and unsaturated alcohols are also known to undergo fragmentation during ionization in the PTR-MS (Brown et al., 2010; Demarcke et al., 2010). Consequently, we cannot rule out that some D_5 VOP fragments are being misattributed in the trends that we report.

For example, methanediol ($CH_2(OH)_2$) is the hydrated form of HCHO and has been observed to largely fragment to a -H_2O PTR ion that overlaps at m/z 31 (Franco et al., 2021). Although $CH_2(OH)_2$ may be formed in the gas phase through HCHO + H_2O via HCOOH catalysis (Hazra et al., 2013), the gaseous compound is thought to have evaporated after being formed heterogeneously (Franco et al., 2021). Franco et al. (2021) also fitted the gaseous unimolecular dehydration ($CH_2(OH)_2 \rightarrow$ HCHO + H_2O) rate coefficient $k_{CH2(OH)2}$ to be 8.5×10^{-5} s^{-1}, which gives the species a unimolecular dehydration lifetime of 0.14 days, which is longer than the experiment residence times of the PAM-OFR. The dominant products from $CH_2(OH)_2$ + OH are HCOOH and HO_2 via the decomposition of the RO_2, and so this diol is practically an intermediate between HCHO and HCOOH.

Given the humid PAM-OFR conditions, $CH_2(OH)_2$ may have been present, and the $-H_2O$ fragment ion may have led to the over-quantification of HCHO; the fragmentation of $CH_2(OH)_2$ during the PTR needs to be characterized to constrain this uncertainty. However, Franco et al. (2021) found that $CH_2(OH)_2 + OH$ has a rate coefficient of $k_{CH2(OH)2+OH} = \sim 7.5 \times 10^{-12}$ cm^3 s^{-1}, and so we expect $CH_2(OH)_2$ to have a OH-oxidation lifetime less than that of τ_{res} at the [OH] in the PAM-OFR. Consequently, we do not expect the $CH_2(OH)_2$ $-H_2O$ fragment interference to the HCHO quantification to be large.

S1.6 Upper Limit Estimation of $k_{age,particle}$

Surface and bulk accommodation processes are not explicitly resolved in the kinetic model and $k_{age,particle}$ acts on the concentrations of particle-phase products per unit air volume. To address whether the numerical value of the fitted $k_{age,particle}$ is reasonable, we calculate its upper physical limit as the collision flow of OH onto the particles in one cm^3 of air ($F_{coll,OH}$, cm^{-3} s^{-1}) derived from gas kinetic theory (Pöschl et al., 2007).

$$F_{coll,OH} = \frac{\omega_{OH}}{4} A_{particle}[OH] \tag{S8}$$

Here, ω_{OH} is the mean thermal velocity of OH in cm s^{-1} (Eq. (S6)) and $A_{particle}$ is the particle surface area density (cm^2 cm^{-3}) measured with the SMPS at the outlet of the PAM-OFR. This flow must always be larger than the heterogeneous reaction flow of OH with the particle surface in one cm^3 of air ($F_{het,OH}$, cm^{-3} s^{-1}).

$$F_{het,OH} = k_{age,particle}\, c_{particle}\, [OH] \tag{S9}$$

Accordingly, we find the following condition for $k_{age,particle}$.

$$k_{age,particle} < \frac{\omega_{OH}}{4\, c_{particle}} A_{particle} \tag{S10}$$

Here, $c_{particle}$, (cm^{-3}) denotes the concentration of total SOSiA products in the particle phase in one cm^3 of air. The estimated upper limit $k_{age,particle}$ are summarized in Table S12.

S2 SOSiA Mass Density (ρ_{SOSiA})

In a separate series of experiments, we collected SOSiA filter samples from the PAM-OFR on pre-weighed PTFE filters (47 mm, 2 μm pore, PT48P-KR, MTL, Minneapolis, MN, USA), where we also operated the SMPS. Then, we stored the filter samples in a desiccator placed inside of a temperature and humidity-controlled micro-balance room for a day to remove mass interference from condensed water. Each filter was weighed ten times on a semi-micro balance (± 0.01 mg, ME204, Mettler

Toledo, Columbus, OH, USA), and we calculate the mean ρ_{SOSiA} by dividing the masses of SOSiA (300 – 740 µg) over integrated SMPS volumes.

From five filter samples, we find a mean (± standard deviation) ρ_{SOSiA} of 1.07 ± 0.08 g cm^{-3}. We note that existing publications used discrepant ρ_{SOSiA} values, which are summarized in Table S9. That range includes those representing SOA (Charan et al., 2022) or D$_5$ itself (Janechek et al., 2019). Wu and Johnston (2017) did not explicitly state the ρ_{SOSiA} they used. Han et al. (2022) used particle size and mass data from an SMPS and an AMS to get ρ_{SOSiA} of 1.6 – 1.8 g cm^{-3} for SOSiA from different siloxane precursors. Avery et al. (2023) used the SOSiA elemental ratios from the AMS with the method described by Kuwata et al. (2012) to obtain ρ_{SOSiA} of 1.59 – 1.78 g cm^{-3}.

For reference, Fytas and Wang (1984) measured the density of several methylphenylsiloxane oligomers, which ranged from 0.99 – 1.10 g cm^{-3}, while He et al. (1988) used a polydimethylsiloxane density parameterization based on molecular weight that maximizes to 0.97 g cm^{-3}. Dee et al. (1992) measured the densities of polydimethylsiloxane oligomers and found values between 1 to 1.14 g cm^{-3}. One of the silanols formed in the siloxane degradation process is dimethylsilanediol (DMSD, $C_2H_8O_2Si$), and Mazzoni et al. (1997) calculated DMSD to have a density of 1.023 g cm^{-3} at 20 °C using a group contribution method. Lamers et al. (2021) found that dimethylsiloxane oligomers of varying lengths would have densities of ~1 g cm^{-3}.

While the ρ_{SOSiA} we report are in line with literature siloxane/silanol densities, they are lower than those reported by Han et al. (2022) and Avery et al. (2023). Some of the difference between their and our ρ_{SOSiA} measurements may be explained by the different experiment conditions, such as OH$_{\text{exp}}$, since aerosol density is expected to increase with higher oxygenation (Kuwata et al., 2012; Nakao et al., 2013). Moreover, Han et al. (2022), Avery et al. (2023), and this study uses different methods to measure ρ_{SOSiA}. Lastly, volatile species may have evaporated from the collected particles while the filters were in the desiccator, which would lead to an undermeasurement of the particle masses and thus SOSiA density.

S3 PTR-MS Calibration

For HCHO, we used a paraformaldehyde permeation tube (CAS#30525-89-4, VICI Metronics, Poulsbo, WA, USA) and a calibration gas generator (Model 150 Dynacalibrator, VICI Metronics, Poulsbo, WA, USA) set to 70 °C to produce HCHO calibration gas with ultra-high purity N$_2$ as the carrier gas. To achieve a steady output, we conditioned the permeation tube in the calibration gas generator for a week at the temperature and carrier gas flow rate to be used during the calibration. The HCHO calibration gas was diluted dynamically to achieve target concentrations with zero/humid air and MFCs, and we correct the HCHO quantification for humidity using Eq. (S11) from Vlasenko et al. (2010), where k_{rev} is the fitted reverse

PTR rate coefficient ($cm^3\ s^{-1}$), $[H_2O]_{dry}$ is the H_2O concentration (cm^{-3}) in the drift tube when sample air is dry, $[H_2O]$ is the water concentration (cm^{-3}) in the drift tube when sample air is humid, and Δt is the drift tube reaction time (9.4×10^{-5} s).

$$\frac{\text{Sensitivity}_{\text{meas}}}{\text{Sensitivity}_{\text{dry}}} = \frac{[H_2O]_{dry}\left(1 - e^{-k_{rev}[H_2O]\Delta t}\right)}{[H_2O]\left(1 - e^{-k_{rev}[H_2O]_{dry}\Delta t}\right)} \tag{S11}$$

To obtain $[H_2O]_{dry}$, we follow the method described in Vlasenko et al. (2010), where we fit a quadratic polynomial (Eq. (S12)) to $(H_2O)_2H^+$ (ncps) against the sample air absolute humidity (Fig. S6.B3). Then, we take the fitted y-intercept ($\approx$ 4000) and linearly approximated the corresponding absolute humidity at 2×y-intercept, which comes to be ~0.005 mol/mol. Lastly, we convert the $[H_2O]_{dry}$ mixing ratio to cm^{-3} using the drift tube pressure (2.30 mbar) and temperature (80 °C).

$$I_{(H2O)2H+} = A + Bx + Cx^2 \tag{S12}$$

For HCOOH, a 1 % (w/w) aqueous solution of HCOOH (>98.0 %, CAS#64-18-6, Tokyo Chemical Industry, Tokyo, Japan) was injected into the VOC bulb with a syringe pump and zero/humid air flowing through the bulb. Like Baasandorj et al. (2015), we find the PTR-MS sensitivity at m/z 47 to be affected by humidity, with sensitivity decreasing with higher RH at 137 Td. Consequently, we adjust the HCOOH quantification for H_2O cluster effects with the method outlined in Baasandorj et al. (2015). We fit the parameters in Eq. (S13), where x is $I_{(H2O)2H+}/I_{(H2O)H+}$.

$$\text{Sensitivity} = A \times \left(B_1 exp(C_1 x) + B_2 exp(C_2 x)\right) \tag{S13}$$

S4 Odum two-product Model

Eq. (S14) shows the Odum two-product parameterization (Odum et al., 1996) for aerosol mass yields, in this case for SOSiA. Janechek et al. (2019) and Charan et al. (2022) fitted their data, and we also parameterize the experimental Y_{SOSiA} with the two-product model in Eq. (S14) for comparison. The partitioning coefficient (K, $m^3\ \mu g^{-1}$) is the inverse of the saturation mass concentration C^* ($\mu g\ m^{-3}$), C_{OA} is the OA mass loading ($\mu g\ m^{-3}$), and α is the product yield for each corresponding K. The fitted values and the literature comparison is shown in Fig. S7, and the Y_{SOSiA} have been adjusted for $\rho_{SOSiA} = 1.07$ $g\ cm^{-3}$.

$$Y_{\text{SOSiA}} = C_{\text{OA}} \left(\frac{\alpha_1 K_1}{1+K_1 C_{\text{OA}}} + \frac{\alpha_2 K_2}{1+K_2 C_{\text{OA}}}\right) \tag{S14}$$

We fit the two-product model with the ρ_{SOSiA}-adjusted data from Han et al. (2022), Avery et al. (2023), and all literature values combined, including those we report. The existing literature values and fit two-product model parameters are

summarized in Tables S9 and S10. As shown in Fig. 4, the two-product model parameters provided by Charan et al. (2022) are consistent with those of Han et al. (2022) and Avery et al. (2023) at ambient surface C_{OA} (0 – 30 µg m^{-3}) with low Y_{SOSiA}. However, the two-product model fit of Janechek et al. (2019) predicts less volatile products, resulting in higher Y_{SOSiA} at those C_{OA}. Our two-product model fit predicts more volatile products, which is consistent with that of Charan et al. (2022), Han et al. (2022), and Avery et al. (2023).

However, for the high C_{OA} cases, the literature diverges with experimental Y_{SOSiA} ranging from 10 to 100 % at ~200 µg m^{-3}, and our Y_{SOSiA} yield curve lies between the curves from the literature (Fig. S7). The intercorrelation of OH_{exp} with Y_{SOSiA} is also visible in Fig. S7, where the higher Y_{SOSiA} measurements occur not only when C_{OA} is high, but also as OH_{exp} increases (color scale). The two-product model here does not explicitly account for chemical aging with OH_{exp}, so we use the aging-VBS approach.

S5 Modeling RO$_2$ Pathways with KinSim

A potential explanation for the Y_{SOSiA} discrepancies in the literature is the RO_2 fate, where high [OH] in OFR experiments may have pushed the RO_2 fate towards a pathway that forms more condensing species. However, Alton and Browne (2022) found in their chamber that $RO_2 + HO_2$, $RO_2 + NO$, and unimolecular pathways would yield similar fractions of siloxanol and formate ester, suggesting these pathways make similar products, likely through RO; Alton and Browne (2022) suggests that the dominant products of $RO_2 + HO_2$ are RO, OH, and O_2, instead of ROOH.

In OFR185, the $RO_2 + OH$ pathway is feasible due to high [OH] and the atmospheric relevance of this pathway is debated (Peng and Jimenez, 2020). However, Fittschen (2019) suggests that $RO_2 + OH$ is an atmospherically relevant pathway in low-NO$_x$ environments, and the dominant product is expected to be RO (+ HO$_2$). That being said, Assaf et al. (2018) found that the dominant product of $RO_2 + OH$ is ROOOH for RO_2 with more than 3 carbon atoms, but we are unaware of any documentation of siloxane RO_2 forming ROOOH. The dominance of RO products across RO_2 fates leading to comparable aerosol mass yields has been reported with monoterpene nitrate oxidation as well (Day et al., 2022).

To assess the RO_2 fates in these experiments, we adopt analogous reactions from the literature and added those RO_2 fates into an OFR mechanism template (Peng and Jimenez, 2020) for KinSim 4.16, a chemical kinetics simulator (Peng and Jimenez, 2019). Table S5 shows the additional RO_2 reactions and rate coefficients appended to the OFR mechanism. The results suggest that $RO_2 + HO_2$ and $RO_2 + OH$ pathways dominated across the experiments, but we encounter an issue reconciling the measured OH_{exp} using (2) and the OH_{exp} from KinSim.

To input the 254 and 185 nm photon fluxes (I_{254} and I_{185}) in KinSim, we follow the recommendations in Rowe et al. (2020) with $I_{254max} = 3.0 \times 10^{15}$ cm^{-2} s^{-1} and $I_{185max}:I_{254max} = 0.0664$. Next, we multiply I_{254max} and I_{185max} by 0.1 to account for the shrink wrap lamp covers and by the ratios of the experiment irradiance and O_3 outputs versus the maximum values at 8V (Table S6). However, we find that with the above photon flux inputs, KinSim calculated the OH$_{exp}$ to be too high and [D$_5$]$_{final}$ to be too low compared with measurements, although the modeled [O$_3$] are consistent with measurements (Fig. S9).

Given that we are interested in probing the RO$_2$ fates, we multiply I_{185} and I_{254} by a factor of 0.1 to bring the OH$_{exp}$ and [D$_5$]$_{final}$ in line with measurements. We use I_{185} of $3 \times 10^{11} - 2 \times 10^{12}$ and I_{254} of $1 \times 10^{12} - 3 \times 10^{13}$ cm^{-2} s^{-1} in the case where I_{185} and I_{254} are multiplied by a factor of 0.1, and the initial fluxes are summarized in Table S6. However, this adjustment leads to the output [O$_3$] being underestimated. To assess the impact of the adjustment on RO$_2$ fates, we model both cases where I_{185} and I_{254} are and are not adjusted (Fig. S10).

In both UV flux cases, KinSim finds RO$_2$ + HO$_2$ and RO$_2$ + OH to be the dominant reaction pathways across the experiments (Fig. S10). A potential explanation for the OH$_{exp}$ discrepancy is the formation of secondary products that are also reactive with OH, which are not included in OHR$_{ext}$ calculated with injected D$_5$. Since we observe the formation of OH-reactive species like HCHO and the proposed VOP appear to be removed with OH$_{exp}$, we suspect that the KinSim mechanism is incomplete, and that a more complete mechanism with subsequent OH-reactive species should improve the KinSim calculations.

For these experiments, we expect RO$_2$ + HO$_2$ and RO$_2$ + OH to have been the dominant pathways across the experiments, based on the findings by Alton and Browne (2022) and the KinSim calculations. Avery et al. (2023) also found similar RO$_2$ fates with KinSim for their experiments, and the common product of these pathways is RO. We note that the inclusion of VOP into the OFR mechanism or when calculating OHR$_{ext}$ may be needed to reconcile measured OH$_{exp}$ and model expectations. Peng and Jimenez (2020) suggest that using measured OH$_{exp}$ is preferred over modelled values due to uncertainties in the OFR residence time, mixing, and OH recycling. We also use RO$_2$ reactions and rate coefficients in the OFR mechanism based on those of organics, and that the RO$_2$ fates are subject to change as the D$_5$ + OH system is further constrained.

References

Alton, M. W. and Browne, E. C.: Atmospheric Chemistry of Volatile Methyl Siloxanes: Kinetics and Products of Oxidation by OH Radicals and Cl Atoms, Environ Sci Technol, 54, 5992–5999, https://doi.org/10.1021/acs.est.0c01368, 2020.

Alton, M. W. and Browne, E. C.: Atmospheric Degradation of Cyclic Volatile Methyl Siloxanes: Radical Chemistry and Oxidation Products, ACS Environmental Au, https://doi.org/10.1021/acsenvironau.1c00043, 2022.

Asbach, C., Kaminski, H., Lamboy, Y., Schneiderwind, U., Fierz, M., and Todea, A. M.: Silicone sampling tubes can cause drastic artifacts in measurements with aerosol instrumentation based on unipolar diffusion charging, Aerosol Science and Technology, 50, 1375–1384, https://doi.org/10.1080/02786826.2016.1241858, 2016.

Assaf, E., Schoemaecker, C., Vereecken, L., and Fittschen, C.: Experimental and theoretical investigation of the reaction of RO2 radicals with OH radicals: Dependence of the HO2 yield on the size of the alkyl group, Int J Chem Kinet, 50, 670–680, https://doi.org/https://doi.org/10.1002/kin.21191, 2018.

Atkinson, R.: Kinetics of the gas-phase reactions of a series of organosilicon compounds with hydroxyl and nitrate(NO3) radicals and ozone at 297 +- 2 K, Environ Sci Technol, 25, 863–866, https://doi.org/10.1021/es00017a005, 1991.

Atkinson, R., Baulch, D. L., Cox, R. A., Crowley, J. N., Hampson, R. F., Hynes, R. G., Jenkin, M. E., Rossi, M. J., Troe, J., and Subcommittee, I.: Evaluated kinetic and photochemical data for atmospheric chemistry: Volume II – gas phase reactions of organic species, Atmos Chem Phys, 6, 3625–4055, https://doi.org/10.5194/acp-6-3625-2006, 2006.

Avery, A. M., Alton, M. W., Canagaratna, M. R., Krechmer, J. E., Sueper, D. T., Bhattacharyya, N., Hildebrandt Ruiz, L., Brune, W. H., and Lambe, A. T.: Comparison of the Yield and Chemical Composition of Secondary Organic Aerosol Generated from the OH and Cl Oxidation of Decamethylcyclopentasiloxane, ACS Earth Space Chem, https://doi.org/10.1021/acsearthspacechem.2c00304, 2023.

Baasandorj, M., Millet, D. B., Hu, L., Mitroo, D., and Williams, B. J.: Measuring acetic and formic acid by proton-transfer-reaction mass spectrometry: sensitivity, humidity dependence, and quantifying interferences, Atmos Meas Tech, 8, 1303–1321, https://doi.org/10.5194/amt-8-1303-2015, 2015.

Brown, P., Watts, P., Märk, T. D., and Mayhew, C. A.: Proton transfer reaction mass spectrometry investigations on the effects of reduced electric field and reagent ion internal energy on product ion branching ratios for a series of saturated alcohols, Int J Mass Spectrom, 294, 103–111, https://doi.org/https://doi.org/10.1016/j.ijms.2010.05.028, 2010.

Charan, S. M., Huang, Y., Buenconsejo, R. S., Li, Q., Cocker III, D. R., and Seinfeld, J. H.: Secondary organic aerosol formation from the oxidation of decamethylcyclopentasiloxane at atmospherically relevant OH concentrations, Atmos Chem Phys, 22, 917–928, https://doi.org/10.5194/acp-22-917-2022, 2022.

Coggon, M. M., McDonald, B. C., Vlasenko, A., Veres, P. R., Bernard, F., Koss, A. R., Yuan, B., Gilman, J. B., Peischl, J., Aikin, K. C., DuRant, J., Warneke, C., Li, S.-M., and de Gouw, J. A.: Diurnal Variability and Emission Pattern of Decamethylcyclopentasiloxane (D5) from the Application of Personal Care Products in Two North American Cities, Environ Sci Technol, 52, 5610–5618, https://doi.org/10.1021/acs.est.8b00506, 2018.

Day, D. A., Fry, J. L., Kang, H. G., Krechmer, J. E., Ayres, B. R., Keehan, N. I., Thompson, S. L., Hu, W., Campuzano-Jost, P., Schroder, J. C., Stark, H., DeVault, M. P., Ziemann, P. J., Zarzana, K. J., Wild, R. J., Dubè, W. P., Brown, S. S., and Jimenez, J. L.: Secondary Organic Aerosol Mass Yields from NO3 Oxidation of α-Pinene and Δ-Carene: Effect of RO2 Radical Fate, J Phys Chem A, 126, 7309–7330, https://doi.org/10.1021/acs.jpca.2c04419, 2022.

Dee, G. T., Ougizawa, T., and Walsh, D. J.: The pressure-volume-temperature properties of polyethylene, poly(dimethyl siloxane), poly(ethylene glycol) and poly(propylene glycol) as a function of molecular weight, Polymer (Guildf), 33, 3462–3469, https://doi.org/https://doi.org/10.1016/0032-3861(92)91104-A, 1992.

Demarcke, M., Amelynck, C., Schoon, N., Dhooghe, F., Rimetz-Planchon, J., van Langenhove, H., and Dewulf, J.: Laboratory studies in support of the detection of biogenic unsaturated alcohols by proton transfer reaction-mass spectrometry, Int J Mass Spectrom, 290, 14–21, https://doi.org/https://doi.org/10.1016/j.ijms.2009.11.005, 2010.

Dewil, R., Appels, L., and Baeyens, J.: Energy use of biogas hampered by the presence of siloxanes, Energy Convers Manag, 47, 1711–1722, https://doi.org/https://doi.org/10.1016/j.enconman.2005.10.016, 2006.

Fittschen, C.: The reaction of peroxy radicals with OH radicals, Chem Phys Lett, 725, 102–108, https://doi.org/https://doi.org/10.1016/j.cplett.2019.04.002, 2019.

Franco, B., Blumenstock, T., Cho, C., Clarisse, L., Clerbaux, C., Coheur, P.-F., de Mazière, M., de Smedt, I., Dorn, H.-P., Emmerichs, T., Fuchs, H., Gkatzelis, G., Griffith, D. W. T., Gromov, S., Hannigan, J. W., Hase, F., Hohaus, T., Jones, N.,

Kerkweg, A., Kiendler-Scharr, A., Lutsch, E., Mahieu, E., Novelli, A., Ortega, I., Paton-Walsh, C., Pommier, M., Pozzer, A., Reimer, D., Rosanka, S., Sander, R., Schneider, M., Strong, K., Tillmann, R., van Roozendael, M., Vereecken, L., Vigouroux, C., Wahner, A., and Taraborrelli, D.: Ubiquitous atmospheric production of organic acids mediated by cloud droplets, Nature, 593, 233–237, https://doi.org/10.1038/s41586-021-03462-x, 2021.

Fytas, G. and Wang, C. H.: Studies of siloxane oligomers by depolarized Rayleigh scattering, J Am Chem Soc, 106, 4392–4396, https://doi.org/10.1021/ja00328a017, 1984.

Han, C., Yang, H., Li, K., Lee, P., Liggio, J., Leithead, A., and Li, S.-M.: Secondary organic aerosols from OH oxidation of cyclic volatile methyl siloxanes as an important Si source in the atmosphere, Atmos Chem Phys, 22, 10827–10839, https://doi.org/10.5194/acp-22-10827-2022, 2022.

Hazra, M. K., Francisco, J. S., and Sinha, A.: Gas Phase Hydrolysis of Formaldehyde To Form Methanediol: Impact of Formic Acid Catalysis, J Phys Chem A, 117, 11704–11710, https://doi.org/10.1021/jp4008043, 2013.

He, X. W., Widmaier, J. M., Herz, J. E., and Meyer, G. C.: Competition between polycondensation of α,ω-dihydroxy polydimethylsiloxane and its condensation with alkoxy silane: A kinetic approach, Eur Polym J, 24, 1145–1148, https://doi.org/https://doi.org/10.1016/0014-3057(88)90100-0, 1988.

Janechek, N. J., Marek, R. F., Bryngelson, N., Singh, A., Bullard, R. L., Brune, W. H., and Stanier, C. O.: Physical properties of secondary photochemical aerosol from OH oxidation of a cyclic siloxane, Atmos Chem Phys, 19, 1649–1664, https://doi.org/10.5194/acp-19-1649-2019, 2019.

Kim, J. and Xu, S.: Quantitative structure-reactivity relationships of hydroxyl radical rate constants for linear and cyclic volatile methylsiloxanes, Environ Toxicol Chem, 36, 3240–3245, https://doi.org/https://doi.org/10.1002/etc.3914, 2017.

Kuwata, M., Zorn, S. R., and Martin, S. T.: Using Elemental Ratios to Predict the Density of Organic Material Composed of Carbon, Hydrogen, and Oxygen, Environ Sci Technol, 46, 787–794, https://doi.org/10.1021/es202525q, 2012.

Lamers, B. A. G., de Waal, B. F. M., and Meijer, E. W.: The iterative synthesis of discrete dimethylsiloxane oligomers: A practical guide, Journal of Polymer Science, 59, 1142–1150, https://doi.org/https://doi.org/10.1002/pol.20200649, 2021.

Li, H., Almeida, T. G., Luo, Y., Zhao, J., Palm, B. B., Daub, C. D., Huang, W., Mohr, C., Krechmer, J. E., Kurtén, T., and Ehn, M.: Fragmentation inside proton-transfer-reaction-based mass spectrometers limits the detection of ROOR and ROOH peroxides, Atmos Meas Tech, 15, 1811–1827, https://doi.org/10.5194/amt-15-1811-2022, 2022.

Liu, X., Day, D. A., Krechmer, J. E., Brown, W., Peng, Z., Ziemann, P. J., and Jimenez, J. L.: Direct measurements of semi-volatile organic compound dynamics show near-unity mass accommodation coefficients for diverse aerosols, Commun Chem, 2, 98, https://doi.org/10.1038/s42004-019-0200-x, 2019.

Mazzoni, S. M., Roy, S., and Grigoras, S.: Eco-Relevant Properties of Selected Organosilicon Materials, in: Organosilicon Materials, edited by: Chandra, G., Springer Berlin Heidelberg, Berlin, Heidelberg, 53–81, https://doi.org/10.1007/978-3-540-68331-5_3, 1997.

Nakao, S., Tang, P., Tang, X., Clark, C. H., Qi, L., Seo, E., Asa-Awuku, A., and Cocker, D.: Density and elemental ratios of secondary organic aerosol: Application of a density prediction method, Atmos Environ, 68, 273–277, https://doi.org/https://doi.org/10.1016/j.atmosenv.2012.11.006, 2013.

Odum, J. R., Hoffmann, T., Bowman, F., Collins, D., Flagan, R. C., and Seinfeld, J. H.: Gas/Particle Partitioning and Secondary Organic Aerosol Yields, Environ Sci Technol, 30, 2580–2585, https://doi.org/10.1021/es950943+, 1996.

Otkjær, R. V., Jakobsen, H. H., Tram, C. M., and Kjaergaard, H. G.: Calculated Hydrogen Shift Rate Constants in Substituted Alkyl Peroxy Radicals, J Phys Chem A, 122, 8665–8673, https://doi.org/10.1021/acs.jpca.8b06223, 2018.

Palm, B. B., Campuzano-Jost, P., Ortega, A. M., Day, D. A., Kaser, L., Jud, W., Karl, T., Hansel, A., Hunter, J. F., Cross, E. S., Kroll, J. H., Peng, Z., Brune, W. H., and Jimenez, J. L.: In situ secondary organic aerosol formation from ambient pine forest air using an oxidation flow reactor, Atmos Chem Phys, 16, 2943–2970, https://doi.org/10.5194/acp-16-2943-2016, 2016.

Peng, Z. and Jimenez, J. L.: KinSim: A Research-Grade, User-Friendly, Visual Kinetics Simulator for Chemical-Kinetics and Environmental-Chemistry Teaching, J Chem Educ, 96, 806–811, https://doi.org/10.1021/acs.jchemed.9b00033, 2019.

Peng, Z. and Jimenez, J. L.: Radical chemistry in oxidation flow reactors for atmospheric chemistry research, Chem. Soc. Rev., 49, 2570–2616, https://doi.org/10.1039/C9CS00766K, 2020.

Porter, W. C., Jimenez, J. L., and Barsanti, K. C.: Quantifying Atmospheric Parameter Ranges for Ambient Secondary Organic Aerosol Formation, ACS Earth Space Chem, 5, 2380–2397, https://doi.org/10.1021/acsearthspacechem.1c00090, 2021.

Pöschl, U., Rudich, Y., and Ammann, M.: Kinetic model framework for aerosol and cloud surface chemistry and gas-particle interactions – Part 1: General equations, parameters, and terminology, Atmos Chem Phys, 7, 5989–6023, https://doi.org/10.5194/acp-7-5989-2007, 2007.

Rowe, J. P., Lambe, A. T., and Brune, W. H.: Technical Note: Effect of varying the λ=185 and 254nm photon flux ratio on radical generation in oxidation flow reactors, Atmos Chem Phys, 20, 13417–13424, https://doi.org/10.5194/acp-20-13417-2020, 2020.

Safron, A., Strandell, M., Kierkegaard, A., and Macleod, M.: Rate Constants and Activation Energies for Gas-Phase Reactions of Three Cyclic Volatile Methyl Siloxanes with the Hydroxyl Radical, Int J Chem Kinet, 47, 420–428, https://doi.org/https://doi.org/10.1002/kin.20919, 2015.

Seinfeld, J. H. and Pandis, S. N.: Atmospheric Chemistry and Physics: From Air Pollution to Climate Change, 1203 pp., 2006.

Timko, M. T., Yu, Z., Kroll, J., Jayne, J. T., Worsnop, D. R., Miake-Lye, R. C., Onasch, T. B., Liscinsky, D., Kirchstetter, T. W., Destaillats, H., Holder, A. L., Smith, J. D., and Wilson, K. R.: Sampling Artifacts from Conductive Silicone Tubing, Aerosol Science and Technology, 43, 855–865, https://doi.org/10.1080/02786820902984811, 2009.

Vlasenko, A., Macdonald, A. M., Sjostedt, S. J., and Abbatt, J. P. D.: Formaldehyde measurements by Proton transfer reaction – Mass Spectrometry (PTR-MS): correction for humidity effects, Atmos Meas Tech, 3, 1055–1062, https://doi.org/10.5194/amt-3-1055-2010, 2010.

von der Weiden, S.-L., Drewnick, F., and Borrmann, S.: Particle Loss Calculator – a new software tool for the assessment of the performance of aerosol inlet systems, Atmos Meas Tech, 2, 479–494, https://doi.org/10.5194/amt-2-479-2009, 2009.

Wu, Y. and Johnston, M. V: Aerosol Formation from OH Oxidation of the Volatile Cyclic Methyl Siloxane (cVMS) Decamethylcyclopentasiloxane, Environ Sci Technol, 51, 4445–4451, https://doi.org/10.1021/acs.est.7b00655, 2017.

Xiao, R., Zammit, I., Wei, Z., Hu, W.-P., MacLeod, M., and Spinney, R.: Kinetics and Mechanism of the Oxidation of Cyclic Methylsiloxanes by Hydroxyl Radical in the Gas Phase: An Experimental and Theoretical Study, Environ Sci Technol, 49, 13322–13330, https://doi.org/10.1021/acs.est.5b03744, 2015.

Yu, Y., Liz Alexander, M., Perraud, V., Bruns, E. A., Johnson, S. N., Ezell, M. J., and Finlayson-Pitts, B. J.: Contamination from electrically conductive silicone tubing during aerosol chemical analysis, Atmos Environ, 43, 2836–2839, https://doi.org/https://doi.org/10.1016/j.atmosenv.2009.02.014, 2009.

Ziemann, P. J. and Atkinson, R.: Kinetics, products, and mechanisms of secondary organic aerosol formation, Chem Soc Rev, 41, 6582, https://doi.org/10.1039/c2cs35122f, 2012.

Table S1. Summary of literature D_5 + OH rate coefficients and measurement methods. We used the empirical values to calculate the average k_{D5+OH}. GC-FID: gas chromatography-flame ionization detector. GC-MS: gas chromatography-mass spectrometry. CIMS: chemical ionization mass spectrometry.

Reference	Method	k_{D5+OH} at ~298 K (cm^3 s^{-1})
Atkinson (1991)	CH_3NO_2 + UV in 6400 L Teflon chamber, GC-FID, rate relative to cyclohexane.	1.55×10^{-12}
Safron et al. (2015)	O_3/H_2O + UV in 140 mL quartz chamber, GC-MS, rate relative to cyclohexane.	2.6×10^{-12}
Xiao et al. (2015)	O_3/H_2O + UV in 140 mL quartz chamber, GC-MS, rate relative to trimethylpentane.	2.46×10^{-12}
	Computed with Spartan 10 and Merck Molecular Force Field molecular mechanics.	~~2.90×10^{-12}~~
Kim and Xu (2017)	O_3/H_2O + UV in 134 L SilcoNert-coated stainless steel chamber, GC-MS, rate relative to n-hexane.	1.46×10^{-12}
Alton and Browne (2020)	O_3/H_2O + UV in 1000 L Teflon chamber, CIMS, rate relative to propionic acid/MEK.	2.1×10^{-12}
Average		**2.0×10^{-12}**

Table S2. Summary of PAM OFR experiment conditions.

Experiment	τ_{res} (sec)	Lamp Voltage	RH (%)	T (°C)	O_3 (ppm)	Irradiance ($\mu W\ cm^{-2}$)	Volume mode (nm)	Surface mode (nm)	Aerosol sampling line loss (%)	Particle number concentration (cm^{-3})
1	180	2.4	33.27 ± 0.07	22.44 ± 0.07	2.18 ± 0.02	0.95 ± 0.05	68.5	57.3	8.49	9.17×10^4
2	180	2.4	33.53 ± 0.07	21.09 ± 0.09	2.37 ± 0.02	0.93 ± 0.05	85.1	66.1	6.74	1.21×10^5
3	180	2.4	32.45 ± 0.03	19.84 ± 0.16	2.29 ± 0.03	0.83 ± 0.08	82	66.1	6.96	1.34×10^5
4	180	2.4	82.47 ± 0.20	20.39 ± 0.12	1.80 ± 0.02	0.56 ± 0.05	98.2	79.1	5.82	3.24×10^5
5	180	2.4	81.96 ± 0.11	21.37 ± 0.08	1.98 ± 0.03	0.84 ± 0.08	131	101.8	4.33	3.83×10^5
6	180	2.4	82.34 ± 0.11	21.57 ± 0.06	1.82 ± 0.02	0.61 ± 0.03	151.2	121.9	3.80	3.83×10^5
7	180	8.0	28.67 ± 0.30	21.66 ± 0.22	12.62 ± 0.15	12.36 ± 0.11	88.2	71	6.52	1.60×10^5
8	180	8.0	28.82 ± 0.16	21.63 ± 0.22	10.65 ± 0.12	9.37 ± 0.11	140.7	113.4	4.02	1.84×10^5
9	180	8.0	28.58 ± 0.17	23.08 ± 0.19	11.04 ± 0.05	9.80 ± 0.07	187.7	145.9	3.15	2.14×10^5
10	180	8.0	75.62	21.61	8.88 ±	12.18 ±	121.9	101.8	4.67	4.62×10^5

					0.08	0.08				
			± 0.51	± 0.29						
11	180	8.0	74.91 ± 0.33	23.03 ± 0.18	8.00 ± 0.06	9.68 ± 0.06	151.2	117.6	3.80	5.18×10^5
12	180	8.0	75.64 ± 0.34	23.40 ± 0.20	8.03 ± 0.04	9.67 ± 0.10	194.6	151.2	3.04	6.64×10^5
13	120	2.4	30.57 ± 0.13	20.15 ± 0.14	1.69 ± 0.01	0.87 ± 0.03	51.4	42.9	11.7	6.30×10^4
14	120	2.4	28.97 ± 0.07	21.16 ± 0.08	1.62 ± 0.01	0.84 ± 0.06	55.2	47.8	10.7	5.56×10^4
15	120	2.4	28.48 ± 0.05	21.10 ± 0.06	1.54 ± 0.01	0.69 ± 0.05	57.3	49.6	10.4	4.39×10^4

Table S3. Summary of experiment condensational sinks, LVOC condensation lifetimes, and growth factors calculated with the particle size distribution exiting the PAM-OFR as described in Section S1.3.

Parameters	SOA, LVOC $\kappa = 0.13$, $M = 0.200$ kg mol^{-1}			SOSiA, D$_5$ $\kappa = 0.01$, $M = 0.370$ kg mol^{-1}		
Experiment	CS (s^{-1})	τ_{CS} (s)	Growth Factor	CS (s^{-1})	τ_{CS} (s)	Growth Factor
1	2.57×10^{-2}	38.8	1.02	1.88×10^{-2}	53.3	1.00
2	3.99×10^{-2}	25.1	1.02	2.92×10^{-2}	34.3	1.00
3	3.88×10^{-2}	25.76	1.02	2.84×10^{-2}	35.2	1.00
4	0.173	5.77	1.17	0.101	9.85	1.02
5	0.303	3.30	1.17	0.182	5.50	1.02
6	0.394	2.54	1.17	0.239	4.19	1.02
7	6.68×10^{-2}	15.0	1.02	4.95×10^{-2}	20.2	1.00
8	0.138	7.27	1.02	0.104	9.63	1.00
9	0.250	3.99	1.02	0.192	5.20	1.00
10	0.338	2.95	1.12	0.217	4.61	1.01
11	0.522	1.92	1.12	0.342	2.93	1.01
12	0.913	1.09	1.12	0.605	1.65	1.01
13	1.25×10^{-2}	80.1	1.02	9.06×10^{-3}	110	1.00
14	1.23×10^{-2}	81.3	1.02	8.96×10^{-3}	112	1.00
15	1.01×10^{-2}	99.3	1.02	7.35×10^{-3}	136	1.00

Table S4. Proposed PTR-MS VOP ions and identities. Here, "D" and "T" refer to silicon center atoms bonded to two and three oxygen atoms respectively.

Ion Formula	Ion Unit Mass (m/z)	Description
$[HCHO]H^+$	31	Formaldehyde
$[HCOOH]H^+$	47	Formic acid
$[C_9H_{27}O_5Si_5]^+$	355	$[D_5\text{-}CH_4]^+$ and $[D_4T(OH)\text{-}H_2O]^+$
$[C_8H_{25}O_6Si_5]^+$	357	$[D_3T_2(OH)_2\text{-}H_2O]^+$
$[C_{10}H_{30}O_5Si_5]H^+$	371	$[D_5]H^+$ dominant isotope
$[C_9H_{28}O_6Si_5]H^+$	373	$[D_4T(OH)]H^+$ dominant isotope or H_2O cluster of m/z 355
$[C_8H_{26}O_7Si_5]H^+$	375	$[D_3T_2(OH)_2]H^+$ dominant isotope
$[C_9H_{25}O_7Si_5]^+$	385	$[D_3T_2(OH)(OCHO)\text{-}H_2O]^+$
$[C_{10}H_{28}O_7Si_5]H^+$	401	$[D_4T(OCHO)]H^+$ dominant isotope

Table S5. Reactions and rate coefficients added to the KinSim OFR mechanism template. The rate coefficients (k) have units of $cm^3\ s^{-1}$ and s^{-1} for bimolecular and unimolecular reactions respectively. Ziemann and Atkinson (2012) notes that the rates of RO_2 + RO_2 varies by orders of magnitude depending on the structure of the RO_2 and that the products are uncertain. Here, we assumed that the initial RO_2 from D_5 + OH is analogous to secondary alkyl RO_2. Alton and Browne (2022) proposes the majority product of RO_2 + HO_2 is RO. The RO_2 + OH rate is for the propylperoxy radical (Fittschen, 2019). For isomerization, we used a value in the range of calculated 1,5 H-shift rates in alkanes, which can vary by orders of magnitude depending on the molecule's functionalization (Otkjær et al., 2018).

Reference	Reaction	Products	k
Alton and Browne (2022)	RO_2 + HO_2	$RO + O_2 + OH$ (90 %) $\newline$ ROOH (10 %)	1.7×10^{-11}
Ziemann and Atkinson (2012)	RO_2 + RO_2	$ROH + R{=}O$ $\newline$ $2RO + O_2$ $\newline$ $ROOR + O_2$	5×10^{-15}
Fittschen (2019)	RO_2 + OH	ROOOH $\newline$ $RO + HO_2$	1.4×10^{-10}
Alton and Browne (2022)	RO_2 rearrangement	RO + HCHO	8.0×10^{-3}
Otkjær et al. (2018)	RO_2 isomerization	$R'O_2$	1×10^{-3}
Atkinson et al. (2006)	HCHO + OH	$HO_2 + CO$	8.5×10^{-12}
Atkinson et al. (2006)	CO + OH	$HO_2 + CO_2$	1.5×10^{-13}

Table S6. Input UV fluxes (cm^{-2} s^{-1}) for KinSim.

Experiment	[O$_3$] matched		OH$_{exp}$ matched	
	I_{185}	I_{254}	I_{185}	I_{254}
1	3.441×10^{12}	2.375×10^{13}	3.441×10^{11}	2.375×10^{12}
2	3.741×10^{12}	2.325×10^{13}	3.741×10^{11}	2.325×10^{12}
3	3.615×10^{12}	2.075×10^{13}	3.615×10^{11}	2.075×10^{12}
4	4.038×10^{12}	1.400×10^{13}	4.038×10^{11}	1.400×10^{12}
5	4.442×10^{12}	2.100×10^{13}	4.442×10^{11}	2.100×10^{12}
6	4.083×10^{12}	1.525×10^{13}	4.083×10^{11}	1.525×10^{12}
7	1.992×10^{13}	3.090×10^{14}	1.992×10^{12}	3.090×10^{13}
8	1.681×10^{13}	2.343×10^{14}	1.681×10^{12}	2.343×10^{13}
9	1.743×10^{13}	2.450×10^{14}	1.743×10^{12}	2.450×10^{13}
10	1.992×10^{13}	3.045×10^{14}	1.992×10^{12}	3.045×10^{13}
11	1.795×10^{13}	2.420×10^{14}	1.795×10^{12}	2.420×10^{13}
12	1.801×10^{13}	2.418×10^{14}	1.801×10^{12}	2.418×10^{13}
13	5.534×10^{12}	2.175×10^{13}	5.534×10^{11}	2.175×10^{12}
14	5.304×10^{12}	2.100×10^{13}	5.304×10^{11}	2.100×10^{12}
15	5.042×10^{12}	1.725×10^{13}	5.042×10^{11}	1.725×10^{12}

Table S7. Fit first generation relative molar yields (γ_i) and $k_{\text{VOP}i+\text{OH}}$ of proposed VOP. Here, "D" and "T" refer to silicon center atoms bonded to two and three oxygen atoms respectively.

Proposed VOP	γ_i	$k_{\text{VOP}i+\text{OH}}$ (cm^3 s^{-1})
D$_4$T(OCHO) (*m/z* 401)	0.0514	4.57×10^{-12}
D$_3$T$_2$(OH)(OCHO) (*m/z* 385)	0.518	5.26×10^{-12}
D$_3$T$_2$(OH)$_2$ (*m/z* 357)	0.343	5.73×10^{-12}
D$_4$T(OH) (*m/z* 355)	1.11	7.53×10^{-12}

Table S8. Experimental molar yields of HCHO and HCOOH. As these species are formed in the OFR at an unknown point, there may be some loss through oxidation with OH. Consequently, the OH_{exp} determined with D_5 may not represent the OH_{exp} these VOP experienced.

Experiment	$\Delta HCHO/\Delta D_5$ (ppb/ppb)	$\Delta HCOOH/\Delta D_5$ (ppb/ppb)
1	1.79 ± 0.25	0.94 ± 0.15
2	1.35 ± 0.15	0.69 ± 0.09
3	1.21 ± 0.21	0.52 ± 0.09
4	1.52 ± 0.11	0.90 ± 0.09
5	1.28 ± 0.11	0.83 ± 0.09
6	0.96 ± 0.06	0.62 ± 0.05
7	1.06 ± 0.06	0.68 ± 0.05
8	1.18 ± 0.09	0.80 ± 0.07
9	0.88 ± 0.04	0.60 ± 0.04
10	0.69 ± 0.03	1.27 ± 0.11
11	0.55 ± 0.02	0.84 ± 0.06
12	0.52 ± 0.02	0.68 ± 0.04
13	2.11 ± 0.76	0.98 ± 0.37
14	1.11 ± 0.24	0.49 ± 0.12
15	1.15 ± 0.29	0.45 ± 0.12

Table S9. Summary of low-NO$_x$ SOSiA experiments as reported in the literature. The Y_{SOSiA} and C_{OA} from the literature are multiplied during the analysis by 1.07/(ρ_{SOSiA} used in the reference) to compare with the values from this study. Wu and Johnston (2017) did not provide a ρ_{SOSiA} nor an OH$_{exp}$, and so we assume their ρ_{SOSiA} to be the same used here (ρ_{SOSiA} = 1.07 g cm^{-3}) and calculated OH$_{exp}$ using their estimated ΔD5 and residence time. Moreover, we convert the ΔD$_5$ they report from ppb to µg m^{-3} with 370.8 g mol^{-1}, 298 K, and 1 atm to calculate their Y_{SOSiA}. Janechek et al. (2019) conducted experiments with and without ammonium sulfate (AS) seed and found that the SOSiA mass concentration would increase with the addition of seed aerosol. We re-calculate their OH$_{exp}$ using the ΔD$_5$ they provide. Charan et al. (2022) does not provide a summary of C_{OA}, so we calculate them using the values in their Table 1 at 1 atm, and we use the Y_{SOSiA} from their oxidation flow tube with the particle wall loss corrections. Also, we update their OH$_{exp}$ with their reported ΔD$_5$ and residence times. Han et al. (2022) provided a range of ρ_{SOSiA} of 1.6 – 1.8 g cm^{-3} for a variety of cyclosiloxane precursors, and we use a value of 1.7 g cm^{-3} for the ρ_{SOSiA} adjustment. We also adjust their OH$_{exp}$ using their reported [OH] and ΔD$_5$.

Reference	Experiment Set Up	Y_{SOSiA} (%)	OH$_{exp}$ (s cm^{-3})	C_{OA} (µg m^{-3})	Seed	ρ_{SOSiA} (g cm^{-3})
Wu and Johnston (2017)	PFA photo-oxidation chamber (50 L, τ_{res} = 15 min)	7.9	1.0×10^{11}	1.2	None	N/A, assumed to be the same used here.
		9.9	1.5×10^{11}	3.3	None	
		12.7	1.5×10^{11}	5.6	None	
		14.3	1.8×10^{11}	8.0	None	
		15.8	2.4×10^{11}	12.0	None	
		13.8	1.1×10^{11}	2.3	AS	
		15.1	9.5×10^{10}	3.2	AS	
		17.5	1.1×10^{11}	4.5	AS	
		21.8	1.5×10^{11}	9.6	AS	
		23.1	1.7×10^{11}	12.6	AS	
Janechek et al. (2019)	PAM-OFR (13.3 L, τ_{res} = 2.7 or 3.8 min)	33	2.0×10^{12}	245	N/A	0.959
		27	1.5×10^{12}	94	N/A	
		25	1.6×10^{12}	119	N/A	
		56	1.6×10^{12}	202	N/A	
		27	1.7×10^{12}	76	N/A	
Charan et al. (2022)	FEP chamber (19 m^3)	1.1	9.9×10^{10}	14.	AS	1.52
		4.0	9.3×10^{10}	31.	AS	
		0	4.7×10^{10}	0	AS	
		1.8	4.2×10^{10}	13.	AS	
Charan et al. (2022)	Caltech photo-oxidation flow tube (τ_{res} = 671 s)	1.3	1.5×10^{10}	1.6	None	1.52
		2.0	1.5×10^{11}	21	None	
		6.5	1.6×10^{11}	72	None	
		4.7	2.4×10^{11}	72	None	
		13	4.6×10^{11}	321	None	

		23	5.5×10^{11}	603	None	
		34	6.2×10^{11}	978	None	
		111	1.8×10^{12}	4024	None	
		111	2.0×10^{12}	4091	None	
		97	3.2×10^{12}	1215	None	
		90	3.3×10^{12}	1127	None	
Han et al. (2022)	Environment and Climate Change Canada OFR (16 L, τ_{res} = 2 min)	1.3	5.5×10^{10}	0.3	None	1.6-1.8
		1.3	1.4×10^{11}	1.1	None	
		6.9	3.5×10^{11}	11	None	
		17	5.0×10^{11}	31	None	
		22	6.0×10^{11}	43	None	
		29	6.8×10^{11}	61	None	
		38	9.0×10^{11}	107	None	
		44	1.2×10^{12}	144	None	
		47	1.3×10^{12}	160	None	
		50	1.7×10^{12}	178	None	
		50	1.8×10^{12}	172	None	
		1.3	5.5×10^{10}	0.5	AS	
		0.6	1.4×10^{11}	1.3	AS	
Avery et al. (2023)	PAM-OFR (13.3 L, τ_{res} = 130 s)	1.2	1.15×10^{12}	2.3	None	1.78
		10	2.42×10^{12}	18	None	1.67
		24	3.77×10^{12}	44	None	1.64
		28	4.55×10^{12}	51	None	1.61
		55	5.23×10^{12}	100	None	1.60
		70	6.21×10^{12}	126	None	1.60
		98	8.23×10^{12}	180	None	1.59

Table S10. Odum two-product model fit values. These two-product parameterizations do not account for OH_{exp}. Janechek et al. (2019) and Charan et al. (2022) state the values below, and Charan et al. (2022) provided 2 fits: with/without particle wall-loss corrections. Han et al. (2022) and Avery et al. (2023) did not provide two-product parameterizations, so we fit their data that was adjusted to $\rho_{SOSiA} = 1.07$ g cm^{-3}; the original ρ_{SOSiA} are in Table S9. We also perform a fit with all values, including those in the literature.

Reference	α_1	α_2	K_1	K_2
Janechek et al. (2019) ($\rho_{SOSiA} = 0.959$ g cm^{-3})	0.14	0.82	1.05	0.00207
Charan et al. (2022) ($\rho_{SOSiA} = 1.52$ g cm^{-3})	0.056/0.044	7.7/5.5	0.022/0.027	$4.3 \times 10^{-5}/6.0 \times 10^{-5}$
Han et al. (2022) ($\rho_{SOSiA} = 1.07$ g cm^{-3})	0.4598	1.284	1.432×10^{-2}	8.546×10^{-4}
Avery et al. (2023) ($\rho_{SOSiA} = 1.07$ g cm^{-3})	5.301	9.756	3.161×10^{-4}	4.209×10^{-4}
This paper ($\rho_{SOSiA} = 1.07$ g cm^{-3})	0.2266	0.6864	0.01478	9.611×10^{-4}
All Values ($\rho_{SOSiA} = 1.07$ g cm^{-3})	0.3814	1.631	0.02551	1.965×10^{-4}

Table S11. Fit VBS product mass yields (α_i) and chemical aging rate coefficients ($k_{age,gas}$). The $k_{age,gas}$ is for the aging-VBS model where OH$_{exp}$ is explicitly parameterized with the and "bin-hopping" as described in Sect. 3.2. We perform fits using the data from our experiments and all values, which includes those in the literature. For α_i smaller than 10^{-5}, we mark them as 0.

C^*	0.1	1	10	100	1000	10000	$k_{age,gas}$	$k_{age,particle}$
This study α_i (no aging)	8.47×10^{-4}	0	0.119	0	0.704	0.176	N/A	N/A
This study α_i	4.20×10^{-3}	3.22×10^{-4}	7.33×10^{-3}	9.05×10^{-2}	1.02×10^{-4}	0.898	2.18×10^{-12}	1.99×10^{-12}
This study α_i ($k_{age,particle} = 0$)	1.11×10^{-3}	2.82×10^{-4}	1.41×10^{-2}	6.84×10^{-2}	2.48×10^{-4}	0.916	2.64×10^{-12}	0
All values α_i (no aging)	4.69×10^{-2}	2.31×10^{-5}	0	0	0.953	0	N/A	N/A
All values α_i	1.27×10^{-3}	7.81×10^{-3}	2.10×10^{-3}	7.77×10^{-2}	1.93×10^{-4}	0.911	2.10×10^{-12}	1.98×10^{-12}

Table S12. Experiment particle surface area densities and OH to particle collision flow, which we denote as the maximum observable $k_{age,particle}$. These maximum values are calculated assuming an effective OH uptake coefficient of 1, and the surface area densities are calculated using the particle size distributions measured with the SMPS. The corresponding effective uptake coefficients are calculated from the ratios of the maximum observable $k_{age,particle}$ and the fit $k_{age,particle}$.

Experiment	Surface Area Density (cm^2 cm^{-3})	Max $k_{age,particle}$ (cm^3 s^{-1})	Estimated Uptake Coefficient
1	6.23×10^{-6}	5.50×10^{-12}	0.362
2	9.84×10^{-6}	4.78×10^{-12}	0.416
3	9.56×10^{-6}	4.98×10^{-12}	0.400
4	3.48×10^{-5}	4.25×10^{-12}	0.468
5	6.41×10^{-5}	3.30×10^{-12}	0.603
6	8.64×10^{-5}	2.79×10^{-12}	0.714
7	1.69×10^{-5}	4.23×10^{-12}	0.470
8	3.71×10^{-5}	2.89×10^{-12}	0.688
9	7.22×10^{-5}	2.19×10^{-12}	0.907
10	7.63×10^{-5}	3.31×10^{-12}	0.601
11	1.24×10^{-4}	2.73×10^{-12}	0.730
12	2.28×10^{-4}	2.19×10^{-12}	0.910
13	2.97×10^{-6}	7.00×10^{-12}	0.284
14	2.95×10^{-6}	6.57×10^{-12}	0.303
15	2.42×10^{-6}	6.02×10^{-12}	0.331
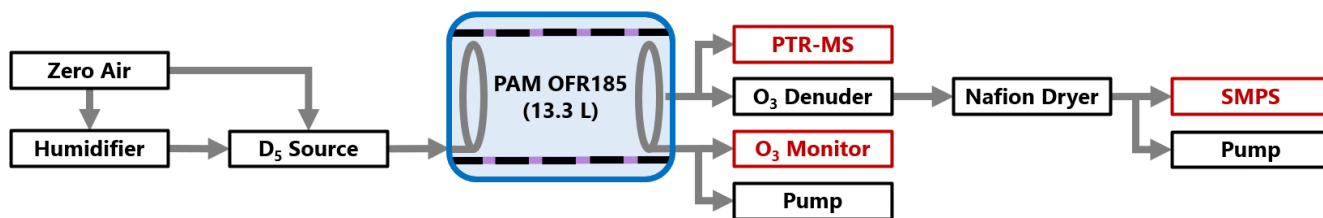
Figure S1. PAM-OFR experiment set up. The D$_5$ source was a syringe pump injecting into a passivated glass bulb. The side ports were equipped with conductive Teflon flow rings on both ends of the PAM-OFR. We covered 90 % of the 185 nm UV lamps to achieve lower irradiances and OH$_{exp}$. We conducted experiments at τ_{res} = 120 s with 6.65 L min^{-1} or 180 s with 4.43 L min^{-1} respectively.
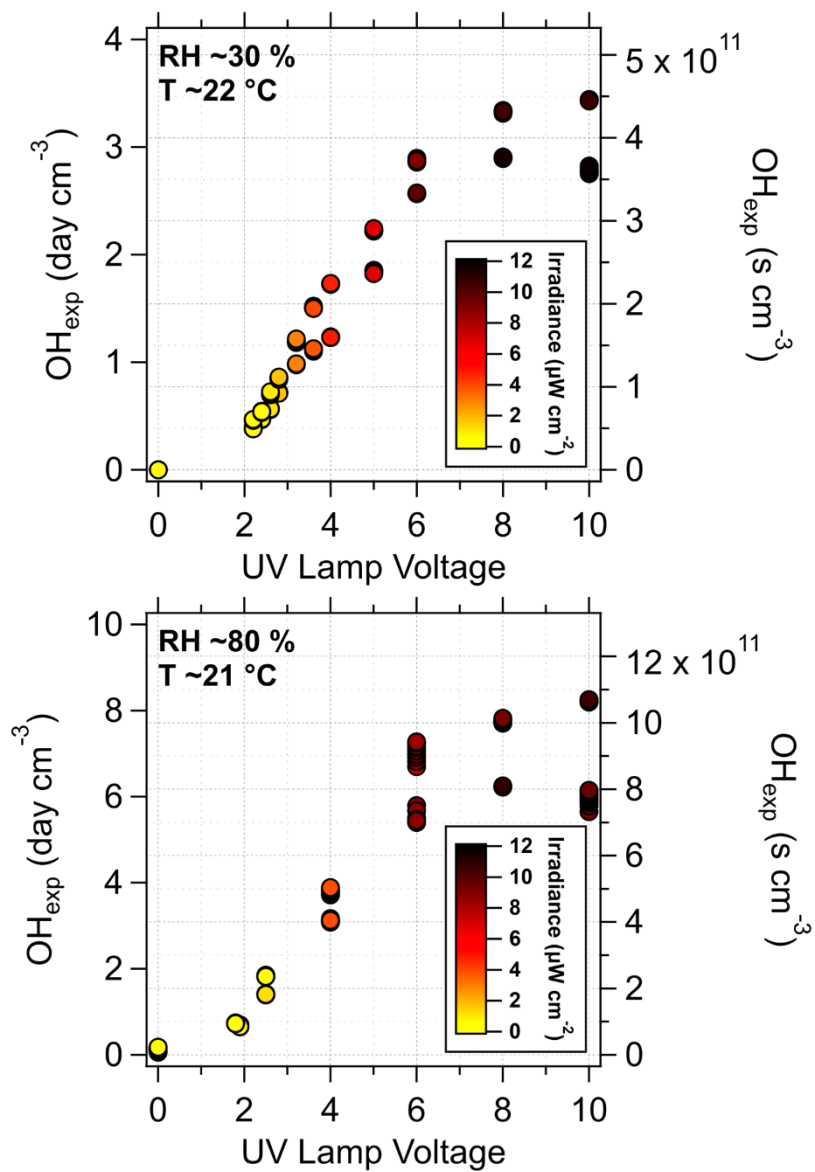
Figure S2. Offline OH$_{exp}$ calibrations with CO at low and high humidity conditions. The OH$_{exp}$ measured during experiments with D$_5$ were consistent with the offline calibration values.
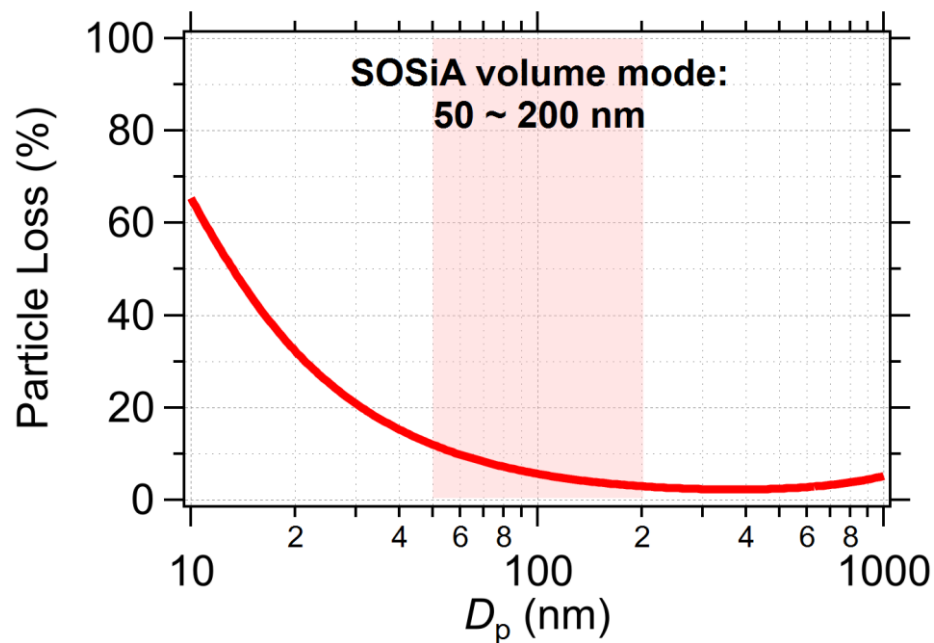
Figure S3. Calculated particle losses with diameters (von der Weiden et al., 2009) using the dimensions of the aerosol sampling line. The shaded area refers to the aerosol volume modes found during experiments.
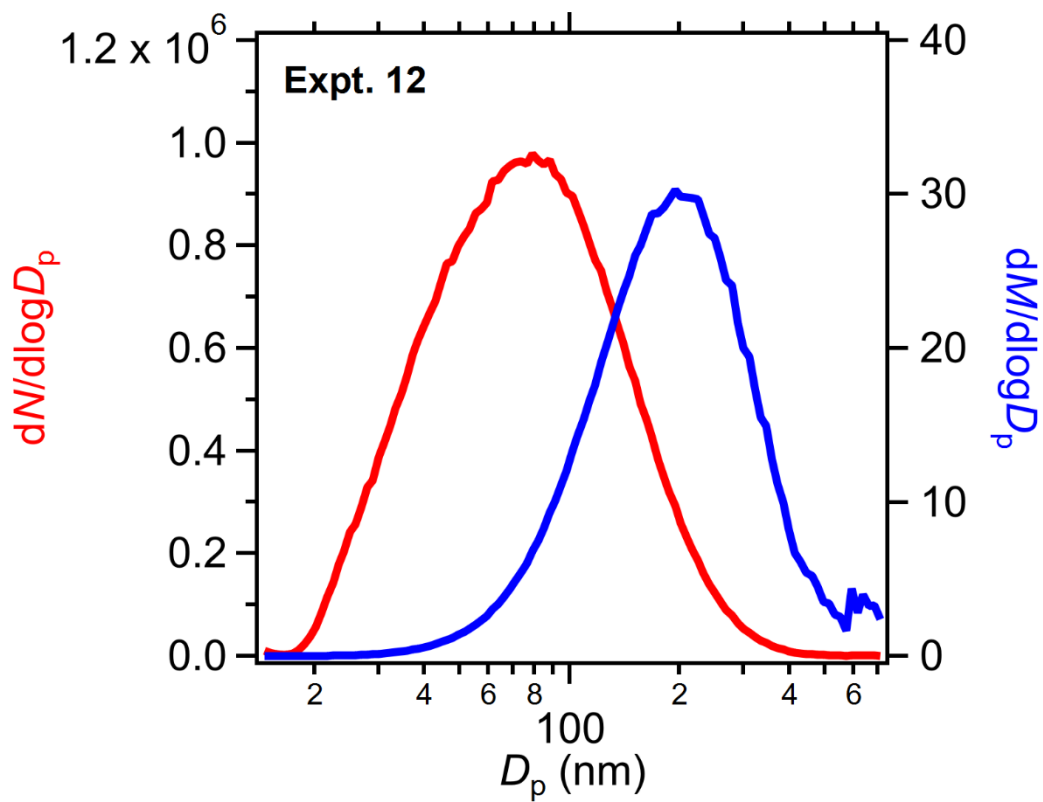
Figure S4. SOSiA particle size distribution for experiment 12, where [D5]0 and OHexp were high.
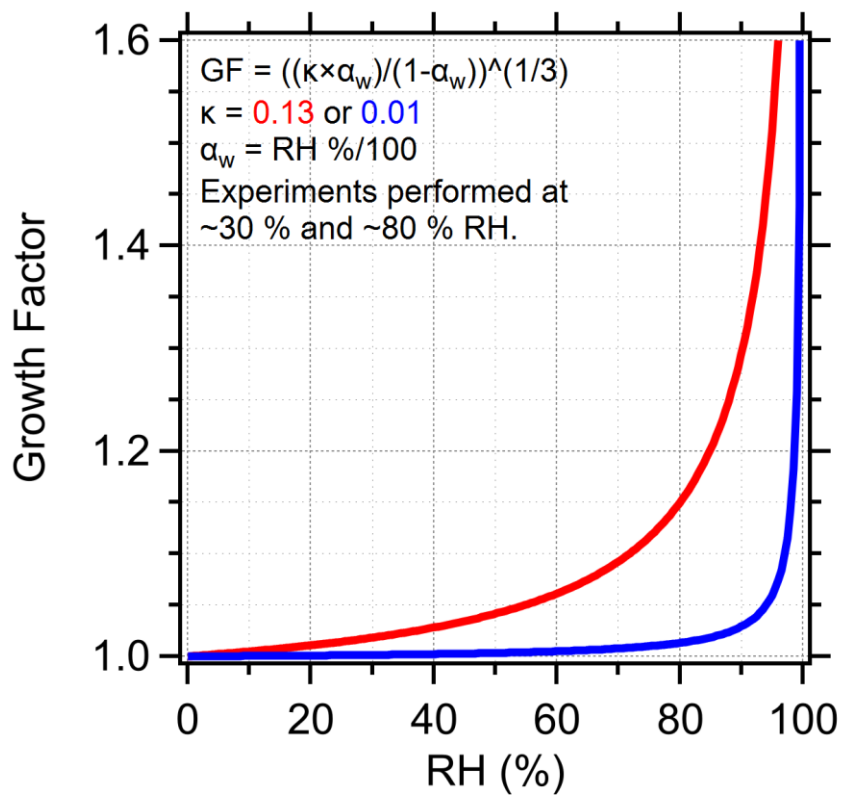
Figure S5. Particle growth factor vs. RH (%) for κ = 0.13 and 0.01. Palm et al. (2016) used the SOA hygroscopicity factor (κ = 0.13), while Janechek et al. (2019) found SOSiA to be non-hygroscopic (κ = 0.01).
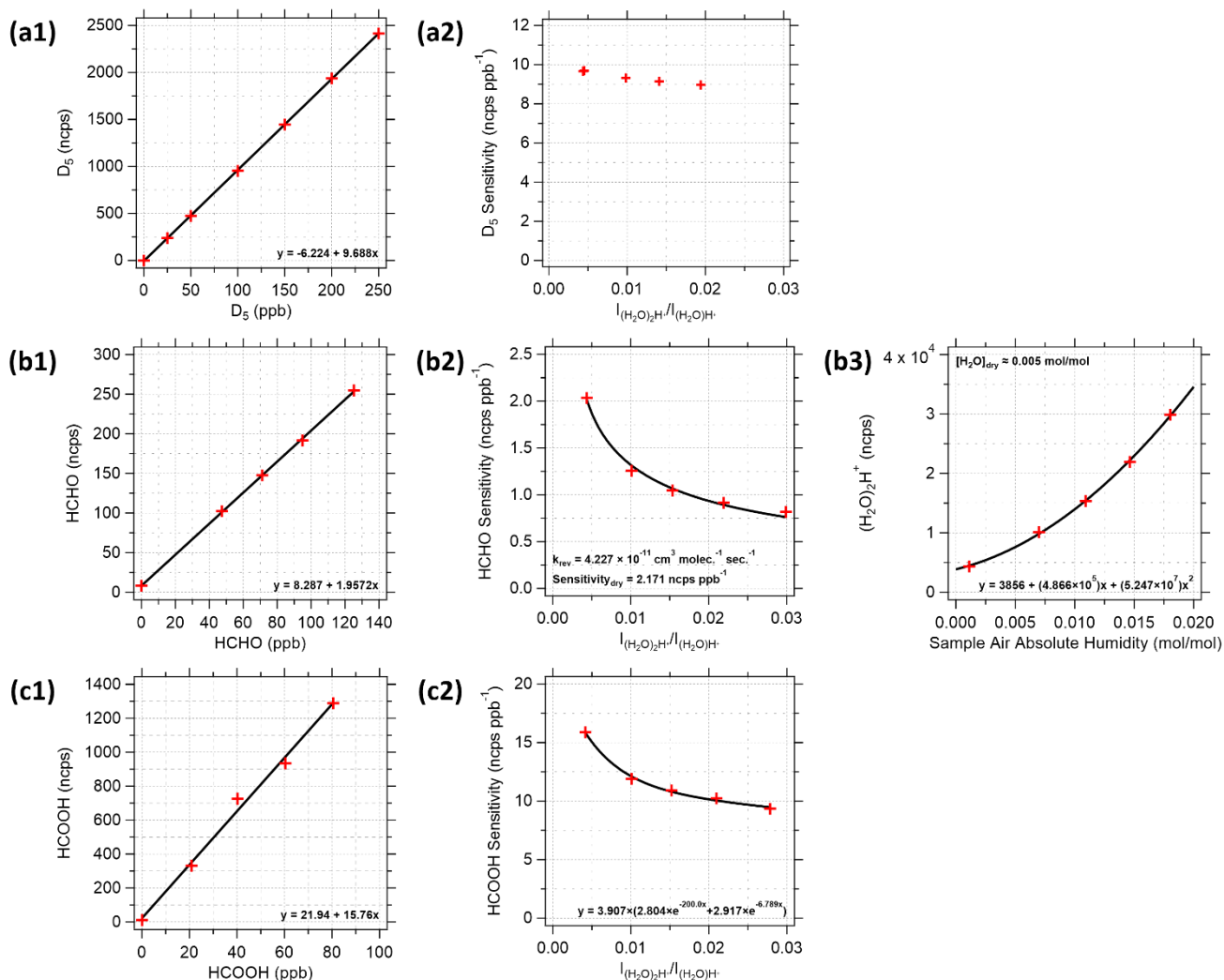
Figure S6. (a1, b1, c1) Calibration curves of D_5, HCHO, and HCOOH. The PTR-MS response was linear under these concentration ranges. **(a2, b2, c2)** Sensitivity variation with humidity. We found the D_5 sensitivity at *m/z* 371 under 137 Td to be consistent with changing humidity and did not apply a correction for the quantification. **(b3)** Polynomial fit to determine the H_2O mixing ratio contribution from the PTR-MS ion source.
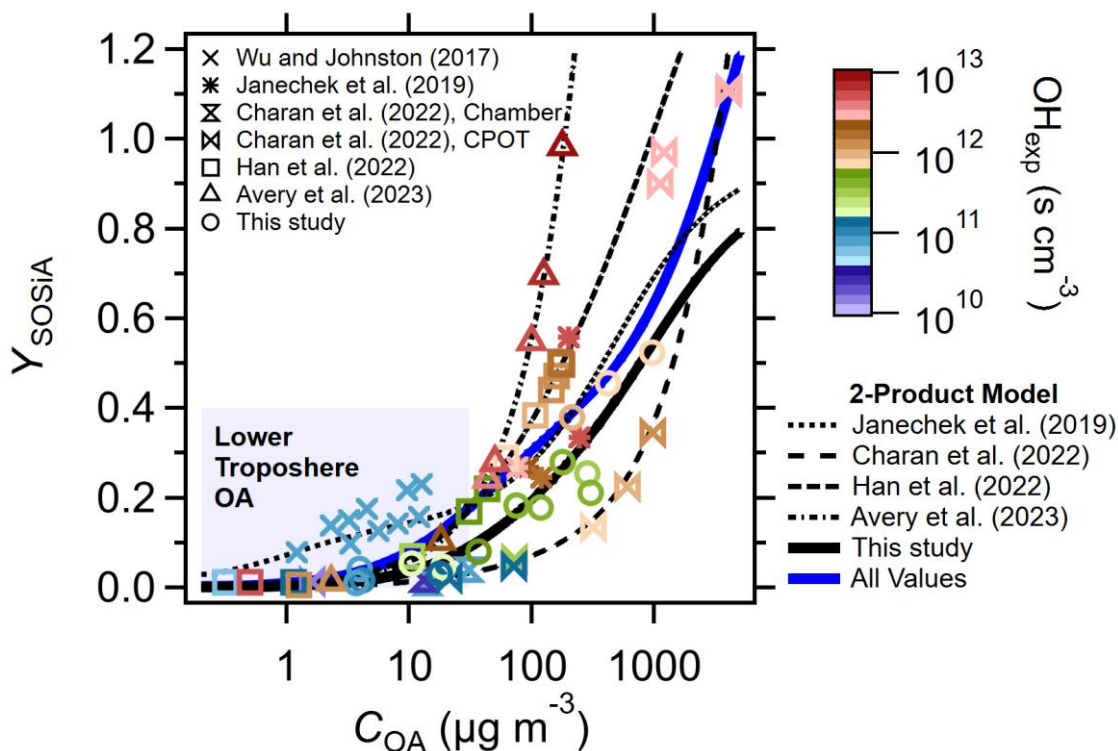
Figure S7 Comparison of Odum two-product model parameterizations between this study and the literature. The blue line is from the fit with all data, including those we report. The shaded area indicates the range of ambient OA concentrations commonly observed in the lower troposphere (Porter et al., 2021). The figure shows the particle wall loss-corrected values from Charan et al. (2022). Han et al. (2022) and Avery et al. (2023) did not provide two-product parameterizations, so we fit the values using their ρ_{SOSiA}-adjusted data (Table S10). Wu and Johnston (2017) did not have measurements of OH_{exp} or D_5 and instead provided estimates. The OH_{exp} (color scale) are those reported by the literature.
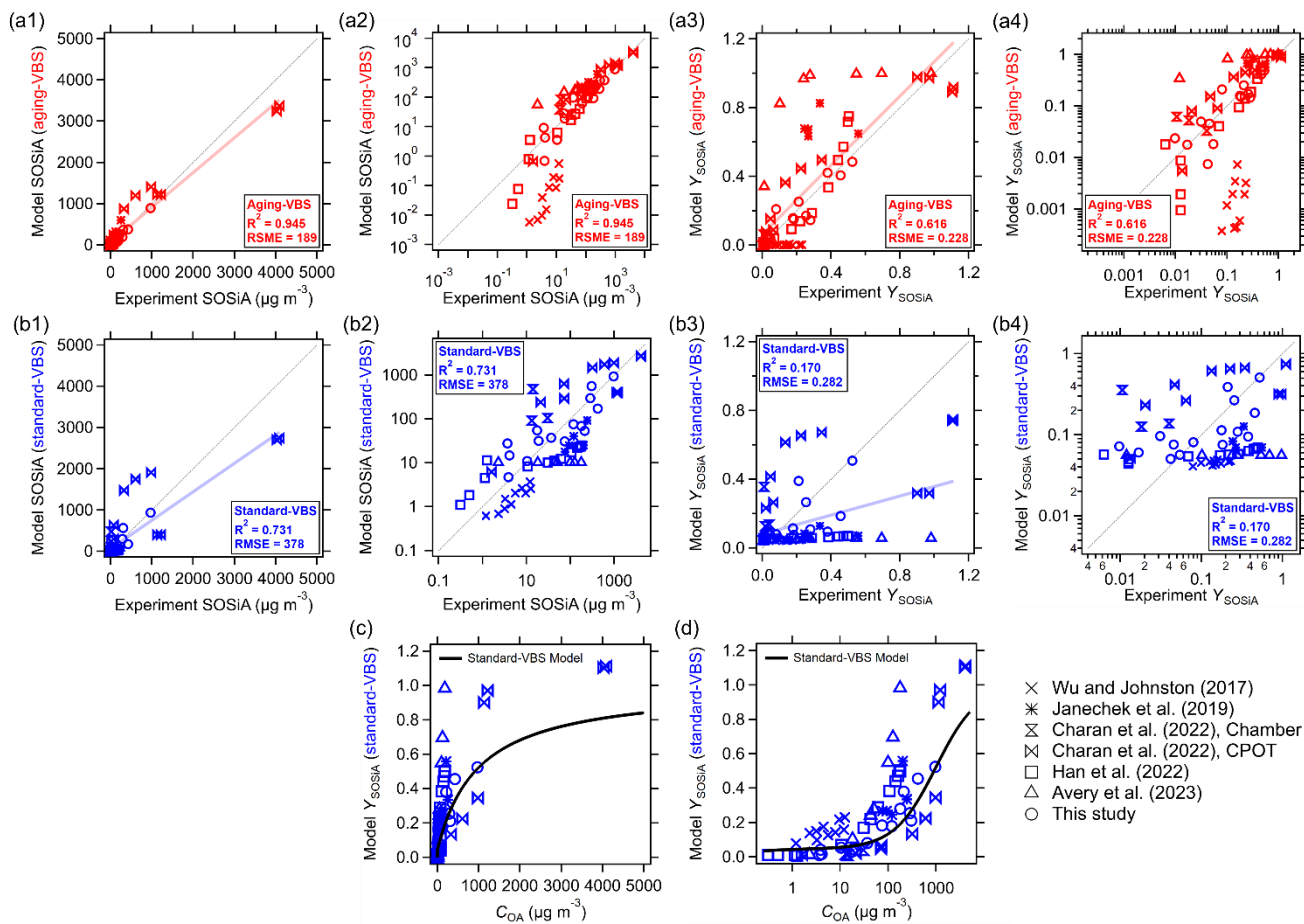
Figure S8. Comparison of the (1, 2) SOSiA mass and (3, 4) Y_{SOSiA} from the (a) aging-VBS and (b) standard-VBS parameterizations fit with values we report and those in the literature (Table S11). Panels (2) show the same data in Panels (1) but in log scale. Panels (c) and (d) show the same Y_{SOSiA} from the standard-VBS model plotted against C_{OA}, but the x-axes are in linear and log scales respectively. The R^2 and root mean square error (RMSE) of the aging-VBS model SOSiA is better than that of the standard VBS.
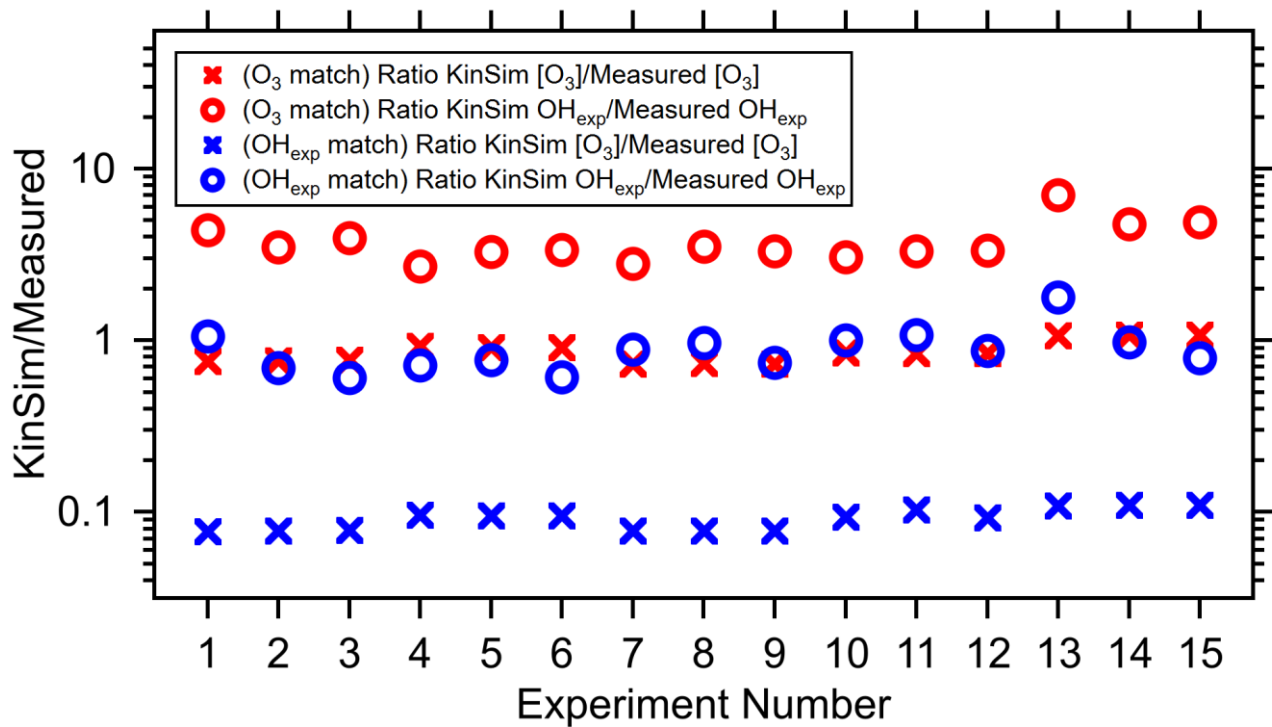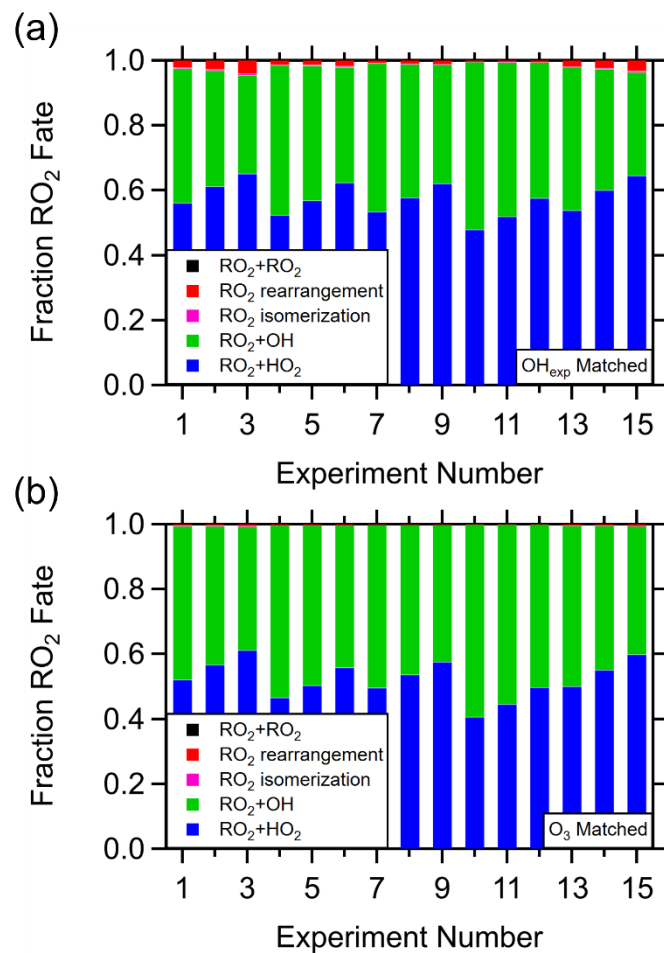
Figure S9. Ratio of the KinSim model outputs vs. measurements for each experiment. The "OH_{exp} match" and "O_3 match" refers to the cases where the UV flux is and is not adjusted so that the KinSim outputs of OH_{exp} and O_3 are in line with measurements respectively.

Figure S10. KinSim estimations of RO₂ fates across experiments. The top panel (a) has I_{254} and I_{185} multiplied by 0.1 (OH$_{exp}$ matched), while the bottom (b) does not (O₃ matched). In both cases, KinSim calculated the RO₂ fates in all experiments to be dominated by the RO₂ + HO₂ and RO₂ + OH pathways.
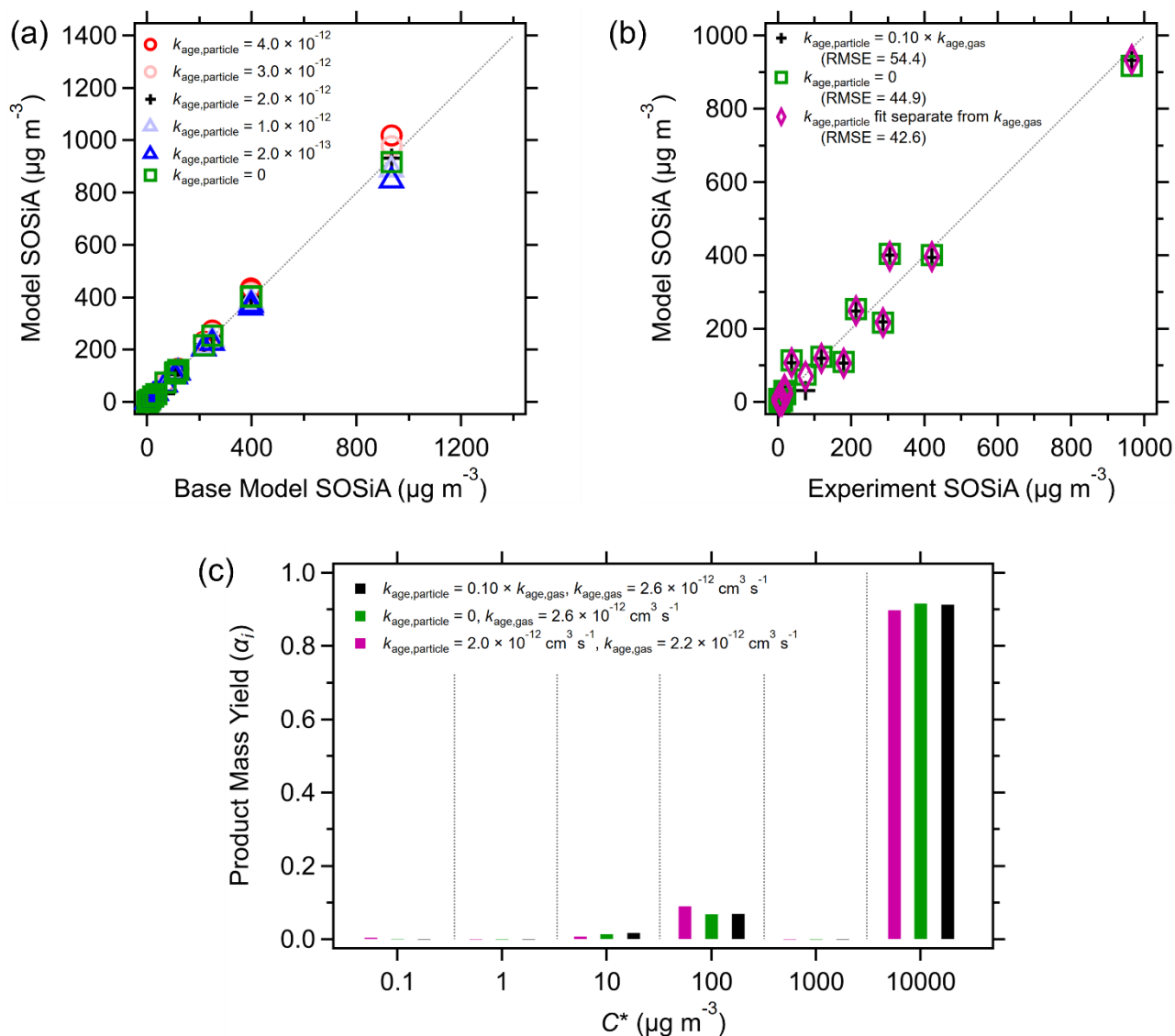
Figure S11. Sensitivity of the aging-VBS model to $k_{age,particle}$: (a) SOSiA formation at varying $k_{age,particle}$ assumptions compared using the optimized parameters found with the "base" model. The base model refers to the version where $k_{age,gas}$ and $k_{age,particle}$ are fit separately. (b) SOSiA formation using optimized parameters found under each $k_{age,particle}$ assumption. The optimized parameters produce comparable RMSE for each corresponding $k_{age,particle}$ assumption. (c) VBS found under each $k_{age,particle}$ assumption. The product mass yields vary only slightly. The purple markers and bars in panels (b) and (c) are from the aging-VBS model used in this paper where $k_{age,gas}$ and $k_{age,particle}$ are fit separately.
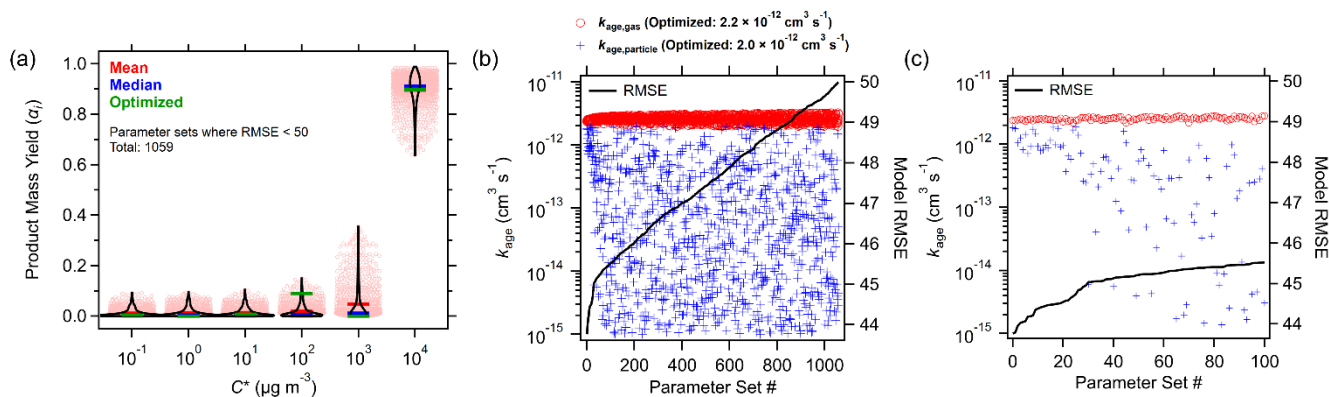
Figure S12. Range of the optimized parameter sets of (a) α_i and (b) the chemical aging rate coefficients in the fit ensemble. Panel (c) shows the same data as panel (b) but only for the 100 best-fitting parameter sets in the fit ensemble. We find a shallow minimum in RMSE for $k_{age,particle}$ around a value of 1×10^{-12} cm^3 s^{-1}. "Optimized" values refer to the best-fit parameter set found with MCGA global optimization. During the global optimization, we generate 768 000 Monte Carlo samples with randomly assigned parameter values. Then, we find the parameter sets where the aging-VBS model outputs RMSE < 50 against SOSiA measurements. We find small variation in the $k_{age,gas}$ while there is large variation in $k_{age,particle}$, suggesting the model is less sensitive to $k_{age,particle}$.